



Premonitory acoustic emissions and stick-slip in natural and smooth-faulted Westerly granite

B. D. Thompson,¹ R. P. Young,¹ and D. A. Lockner²

Received 16 April 2008; revised 8 October 2008; accepted 2 December 2008; published 13 February 2009.

[1] A stick-slip event was induced in a cylindrical sample of Westerly granite containing a preexisting natural fault by loading at constant confining pressure of 150 MPa. Continuously recorded acoustic emission (AE) data and computer tomography (CT)-generated images of the fault plane were combined to provide a detailed examination of microscale processes operating on the fault. The dynamic stick-slip event, considered to be a laboratory analog of an earthquake, generated an ultrasonic signal that was recorded as a large-amplitude AE event. First arrivals of this event were inverted to determine the nucleation site of slip, which is associated with a geometric asperity on the fault surface. CT images and AE locations suggest that a variety of asperities existed in the sample because of the intersection of branch or splay faults with the main fault. This experiment is compared with a stick-slip experiment on a sample prepared with a smooth, artificial saw-cut fault surface. Nearly a thousand times more AE were observed for the natural fault, which has a higher friction coefficient (0.78 compared to 0.53) and larger shear stress drop (140 compared to 68 MPa). However at the measured resolution, the ultrasonic signal emitted during slip initiation does not vary significantly between the two experiments, suggesting a similar dynamic rupture process. We propose that the natural faulted sample under triaxial compression provides a good laboratory analogue for a field-scale fault system in terms of the presence of asperities, fault surface heterogeneity, and interaction of branching faults.

Citation: Thompson, B. D., R. P. Young, and D. A. Lockner (2009), Premonitory acoustic emissions and stick-slip in natural and smooth-faulted Westerly granite, *J. Geophys. Res.*, 114, B02205, doi:10.1029/2008JB005753.

1. Introduction

[2] Observations of dynamic instabilities on laboratory faults have proven extremely valuable in improving the understanding of earthquake nucleation, since the proposal by *Brace and Byerlee* [1966] that the mechanism of stick-slip in the laboratory was identical to that of earthquakes on faults. Further, the rate and state dependant constitutive friction laws that resulted from laboratory measurements [*Dieterich*, 1978, 1979; *Ruina*, 1983] have been applied to many seismic observations (as reviewed, for example, by *Lockner and Beeler* [2002]). *McGarr* [1999] considers that scaling of laboratory stick-slip values to the field can provide valuable insights into earthquake processes for a wide range of hypocentral environments. Indeed, recent recordings of microseismicity in South African gold mines [*Boettcher et al.*, 2007] have shown mining-induced seismicity below M-3.0 which overlaps the energy release of laboratory-scale stick-slip events. *Rice and Cocco* [2007] discuss the possibility that laboratory measurements require no scaling but can be applied directly to the Earth to represent local fault behavior.

[3] Faults tend to be geometrically complex, and a motivation of this experiment was to explore, in the laboratory, the difference between irregular, naturally formed faults and the planar saw-cut fault surfaces that are commonly used in the laboratory. *Ben-Zion and Sammis* [2003] describe the San Andreas system as consisting of several major subparallel faults with a network of subsidiary faults that have complex geometry. On a smaller scale, the main trace of the fault contains a core of crushed rock, often with anastomosing shear surfaces, surrounded by zones of intense fracturing. Bends and jogs along the main fault strands also add to complexity. Observations of the complexity of active faults have resulted from improvements in the resolution of small magnitude seismicity. Microseismicity, previously thought to be distributed over large portions of creeping faults has been shown by *Rubin et al.* [1999] to localize in highly concentrated streaks, aligned with the slip direction. High-resolution locations of microseismicity reported by *Waldhauser and Ellsworth* [2002] provided details of the structure and mechanics of the Hayward Fault in California, suggesting that the large seismic regions between streaks of small magnitude seismicity represent locked zones. Thus faults appear to contain significant geometric disorder and zones with heterogeneous properties. Such features can provide barriers to rupture propagation, can generate slip complexities and can enable isolated high-stress regions to exist, while the remainder of the fault is under conditions of low shear stress [*Ben-Zion*, 2001].

¹Department of Civil Engineering, Lassonde Institute, University of Toronto, Toronto, Ontario, Canada.

²U.S. Geological Survey, Menlo Park, California, USA.

[4] In large-scale biaxial tests, the nucleation process for stick-slip events have been measured using high-speed records of shear strain and slip velocity [Dieterich, 1978; Okubo and Dieterich, 1984; Ohnaka and Kuwahara, 1990]. Ohnaka and Kuwahara [1990] summarized the nucleation of instability as a three stage process consisting of (1) the static formation of a slip failure nucleus, (2) the subsequent quasi-static steady crack growth, and (3) the quasi-static but accelerating crack growth to a critical crack length, at which instability occurs. Okubo and Dieterich [1984] compared a smooth and a rough fault surface (with surface roughness $0.2 \mu\text{m}$ and $80 \mu\text{m}$ respectively) at normal stresses between 0.6 and 4 MPa. Critical slip distance D_c , was measured and found to be insensitive to normal stress, however it increased with fault roughness ($5 \mu\text{m}$ and $25 \mu\text{m}$ respectively). D_c is thought to correspond to a characteristic length scale of surface topography. However, there is an inconsistency between D_c measured on the laboratory scale and on field scales. One suggested reason for this discrepancy is that the preparation of laboratory fault surfaces can impart a characteristic length scale, unlike the fractal geometry measured for natural faults [Brown and Scholz, 1985; Power et al., 1987]. In order to better understand the complexities of faulting, previous experiments have considered fault bends [Kato et al., 1999], heterogeneities in normal stress [Yoshida and Kato, 2001], and the rupture of jointed samples under triaxial compression [Lei et al., 2003, 2004]. These studies demonstrated the importance of asperities or stress concentrators in the rupture process.

[5] Thompson et al. [2005] considered stick-slip behavior on a homogenous fault plane, for a sample containing a saw-cut and polished fault. Continuous AE was recorded in order to determine details of slip nucleation, and premonitory AE characteristics. We extend this work to consider stick-slip in a sample containing a quasi-statically propagated fault surface. This sample better approximates a natural fault zone in terms of its geometrical complexity, which includes branching secondary faults and nonplanar fault topography, and in the absence of a mechanically induced characteristic length scale. AE source locations are used to monitor the spatial and temporal evolution of microscale fracturing and the nucleation site of the stick-slip event. Further, high-resolution X-ray computed tomography (CT) images are produced in order to relate AE to phases of microscale damage within the sample. Previously Lei et al. [2004] and Benson et al. [2007] have demonstrated the benefit of combining AE locations with CT images.

[6] Continuous ultrasonic waveforms have been recorded using very similar experimental conditions for frictional slip and also for failure in intact samples [Thompson et al., 2006]. Given the similarities in the nucleation processes for frictional slip and intact fracture [Ohnaka, 2003; Thompson et al., 2006] we extend the comparison of slip on a natural and smooth fault to include the characteristics of ultrasonic emissions previously associated with failure of intact rock.

2. Method

2.1. Experimental Procedure

[7] A “natural” fracture was created in a room dry, intact cylindrical sample (190.5 mm length, 76.2 mm diameter) of Westerly granite using a triaxial loading system at constant

confining pressure of $P_c = 50 \text{ MPa}$. The sample, jacketed in a polyurethane sleeve, was loaded using an AE feedback regime in order to suppress the normal dynamic rupture process and instead produce quasi-static development of the through-going fault surface. This procedure is comprehensively described by Thompson et al. [2006]. Following fault formation in the initially intact sample, the confining stress was increased and a dynamic stick-slip rupture was induced on the fault surface.

[8] The stick-slip phase of the experiment began with an initial loading cycle at a confinement of 200 MPa and reached an axial stress of 740 MPa without slip on the fault. In order to reduce the risk of damage to the instrumentation, differential stress was removed and a second loading cycle was performed at $P_c = 150 \text{ MPa}$. This loading cycle culminated in the stick-slip event reported here. During this phase, axial stress was increased under servo-control at a constant strain rate (measured with a displacement transducer outside the pressure vessel) of $5 \times 10^{-6} \text{ s}^{-1}$.

2.2. Geometry of the Natural Fault

[9] The geometry of the fault prior to the stick-slip experiment is illustrated using AE source locations that are superimposed onto CT images of the postslip sample in Figure 1. The CT image is approximately perpendicular to the main fault plane, passing through the central axis of the sample with a strike of $N85^\circ E$ (referenced to the transducer array). AE are selected for a volume extending $\pm 10 \text{ mm}$ from the plane of the CT image. In Figure 1a, AE events are shown that were recorded during fault growth in the initially intact sample. These AE events delineate two quasi-statically propagated fractures. The first fracture nucleated on the surface of the sample and propagated upward to the loading platen. A second fracture then propagated downward through sample. This second through-going fracture was the main surface along which displacement occurred and is referred to as the main fault. Its “S” shape is a common feature in granite samples fractured under triaxial loading conditions. Other faults are conjugate fractures probably formed because of significant stress concentrations at the inflection points of the main fault and are referred to as secondary faults. Figure 1b shows AE resulting from the increase in confining pressure (from 50 to 200 MPa) after the quasi-static growth of the main fault, but before reapplication of axial load. AE in the upper east quadrant relate to the quasi-statically propagated fracture that intersects the rock-loading platen boundary. The CT image indicates the diffuse distribution of events in the lower west quadrant relate to a highly fractured region. This is identified as a new region of damage that was generated during the fracture of the intact sample.

2.3. AE Setup

[10] Seventeen piezoelectric transducers of diameter 7 mm and resonant frequency 800 kHz were directly attached to the sample. Thirteen transducers were used as receiving transducers and four as transmitting sources for determining wave speed evolution during the experiment. Further details of the transducer response characteristics can be found in the work of Stanchits et al. [2003]. The output from all receivers was amplified by 40 dB and for two receivers the

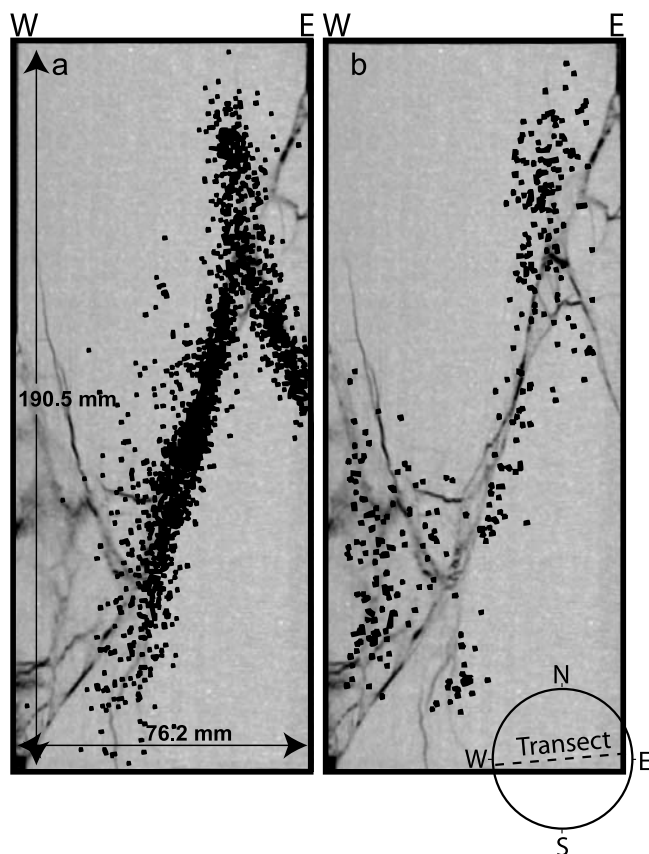


Figure 1. Source locations for AE induced by (a) quasi-static fracture of the intact sample and (b) the later increase in confining stress prior to the stick-slip loading cycles. These locations demonstrate fault geometry prior to the stick-slip experiment. AE locations are superimposed onto a reconstructed CT image of the postslip sample, which is oriented at an 85° angle from the north, across the diameter of the sample, perpendicular to the strike of the main fault plane. AE locations (described in the text) are shown for a volume extending ± 10 mm from the plane of the CT image. CT images were produced at the High-Resolution X-ray Computed Tomography Facility of the University of Texas at Austin.

raw output was also amplified by 20 dB to provide a broader dynamic range. Full waveform AE data were recorded using the Giga RAM Recorder [Thompson *et al.*, 2006]. In this system, data are digitized at 14-bit resolution, with an input voltage range of ± 2.5 V, and are continuously streamed to a 40 GB RAM buffer that can be locked for later download following an important period in an experiment. In this test, a sampling rate of 5 MHz was used which equates to a 268-s segment of continuous waveform data. Triggered AE waveform data were recorded throughout the test, with each event having a trace length $204.8 \mu\text{s}$, and a maximum capacity of 16 events per second. Finally the number of amplitude threshold crossings was recorded at each sensor. This is termed the AE “Hit” count to distinguish between this and the numbers of full waveform triggered AE. The loading apparatus and AE acquisition set up has previously been described in detail by Thompson

et al. [2006], and is schematically shown along with details of the fracture geometry in Figure 2. Sensor locations on the sample are shown in Figure 3.

2.4. Acoustic Emission Data Processing

[11] Two AE catalogues are considered. Firstly, discrete AE events were recorded throughout the experiment if the amplitude measured on five or more channels exceeded a 75 mV threshold within a $50 \mu\text{s}$ window. Secondly, the complete catalogue of discrete AE was extracted by applying the above trigger logic to the continuously streamed ultrasonic waveform data which includes 102 s of activity before the slip event. The disadvantage of recording triggered AE is that downtime is experienced while events are transferred from RAM to permanent storage, and so events that satisfy the triggering threshold criterion can be lost during periods of significant AE activity. This limitation is removed by recording continuous data. A further advantage is that the continuous waveform can be revisited to optimize the amplitude threshold above which discrete events are extracted.

[12] AE source locations were calculated using a Simplex algorithm [Nelder and Mead, 1965] using first arrival times selected using an automated routine. A transversely isotropic velocity structure was used in the location routine. In order to ensure accurate locations, the residual difference between the measured and theoretical travel time from the source location was calculated for each channel. If the residual exceeded $1.0 \mu\text{s}$, the channel was dropped from the location algorithm. Source locations calculated using fewer than 7 arrivals were discarded. A method for estimating approximate AE location accuracy was employed in which source transducers at known locations on the sample surface were pulsed. The resultant arrival time data at the receiver array were inverted for the source locations and gave a mean error of 4 mm. However, as discussed by Thompson *et al.* [2006], it is thought that accuracy improves by up to 50% for AE sources occurring in the interior of the sample.

[13] Source mechanisms for selected AE were calculated by inverting P wave first arrival amplitude data to provide time-independent moment tensor (MT) solutions. The MT approach used in this study is described by Collins *et al.* [2002] and was previously used by Thompson *et al.* [2005]. Data from two periods of the experiment are considered. Each data catalogue was sorted and processed in order of largest magnitude until 20 solutions were obtained. This strategy enables a like-for-like comparison of the largest events and ensures events have high signal to noise ratios. Good focal coverage is important, and so only events from the central third of the sample (i.e., between 63 and 126 mm from the base of the sample) were considered. In order to provide more accurate results the data was processed manually. All solutions have 9 or more arrivals and the residual between the modeled and observed amplitudes was used to check the quality of the inversion. Finally, the stability of each inversion was tested by dropping random arrivals. For the case where the dynamic range of the system was exceeded and amplitude data was unavailable, first motion polarities were used to calculate the fault plane solution using a probability based routine modified from the

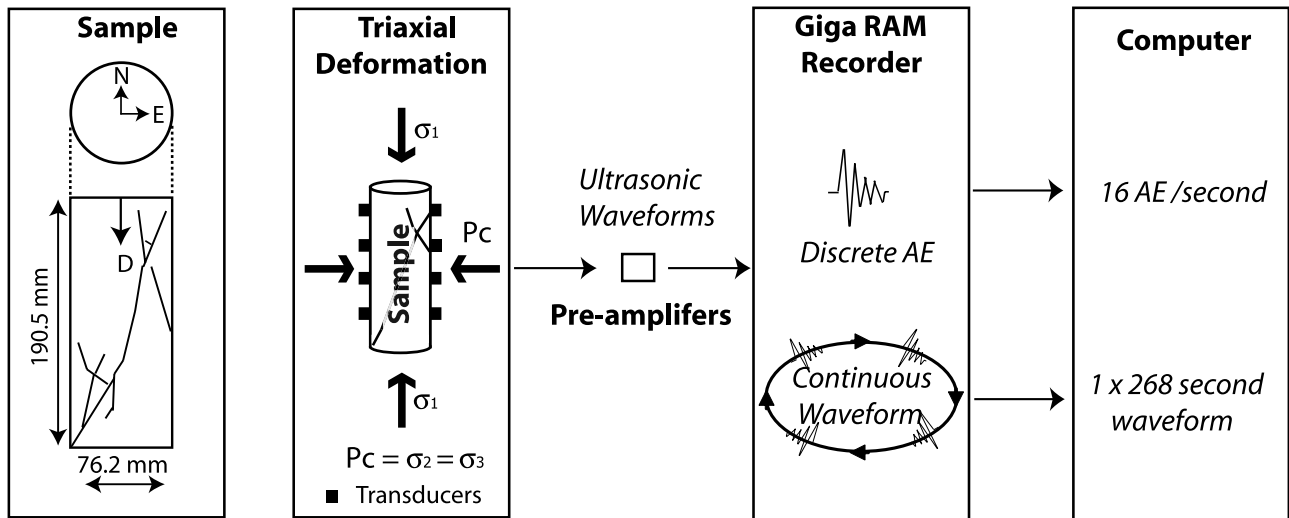


Figure 2. Schematic diagram of the experimental setup, including (from left to right) the sample and preexisting fracture geometry (interpreted from Figure 1) with coordinate system marked (north, east, down), the triaxial load configuration, and acquisition capabilities of the Giga RAM Recorder.

work of *Udias and Buforn* [1988], assuming a double couple source.

2.5. X-ray Computed Tomography

[14] The sample, still contained within the polyurethane jacket, was imaged at the High-Resolution CT Facility at the University of Texas at Austin. The high-energy scanning system was used, which was designed to image large samples, and employs a 420-kV tungsten X-ray source. Images are obtained horizontally across the 76.2 mm sample diameter for 1 mm thick slices at a resolution of 488×488 pixels, and 0.5 mm interslice spacing. This resolution is sufficient to enable identification of features larger than approximately 0.5 mm in length. The images are processed for streak and ring removal, and the image is reconstructed to provide views along strike and perpendicular to the strike of the main fault plane. *Louis et al.* [2006] use high-quality CT images from the same facility to investigate compaction band formation. Further details of the facility and techniques employed are contained in the work of *Ketcham and Carlson* [2001].

3. Results

3.1. Mechanical Data

[15] The main stick-slip instability was induced in this experiment at a differential stress (= axial stress – confining pressure) of 476 MPa at time 9826 s. Shear (τ) and normal (σ_n) stresses are resolved along the $\sim 65^\circ$ fault plane as 182 MPa and 235 MPa respectively, and the coefficient of friction (τ/σ_n) is 0.78. Figure 4a shows the axial stress, confining pressure and AE hit count and Figure 4b shows differential stress versus axial strain. A small but audible 2.7 MPa dynamic stress drop occurred 220 s before the stick-slip on the main fault and is discussed later. For clarity, the earlier dynamic event is termed “the 2.7 MPa event” and the later, main stick-slip is referred to as “the stick-slip”. The stick-slip ended at 22.2×10^{-3} strain as plotted in

Figure 4b. The apparent dynamic strain would then be $\epsilon_B = 6.5 \times 10^{-3}$ (1.2 mm axial displacement). However, the strain released by the elastic rebound of the sample ($\epsilon_A = 10.7 \times 10^{-3}$) should be corrected for, and so the true dynamic strain is $\epsilon_A + \epsilon_B = 17.2 \times 10^{-3}$ (3.3 mm axial displacement). Resolved on the fault plane, total dynamic slip is calculated to be 3.6 mm. The dynamic shear stress drop, resolved on the fault plane, was 140 MPa implying an unloading stiffness of $k = 43$ MPa/mm.

[16] We end this section with an estimate of the moment magnitude of the stick-slip event in terms of an equivalent

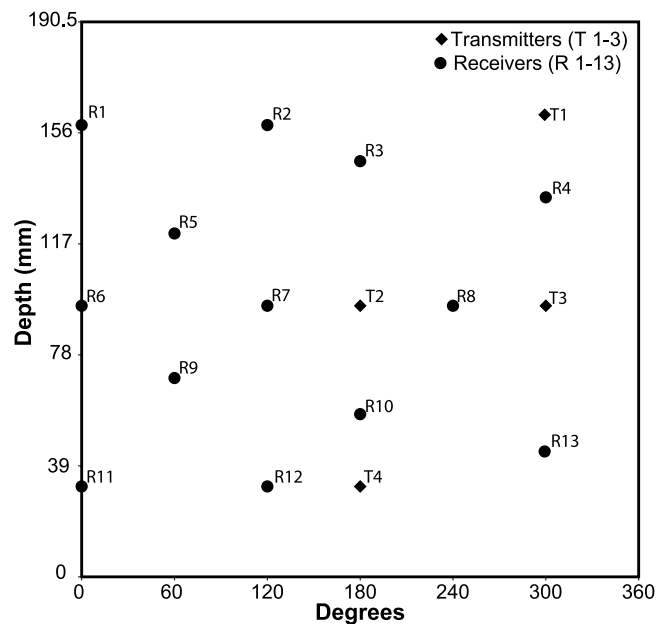


Figure 3. Map of receiving and transmitting transducer locations on the sample plotted for sample height against degrees from the north.

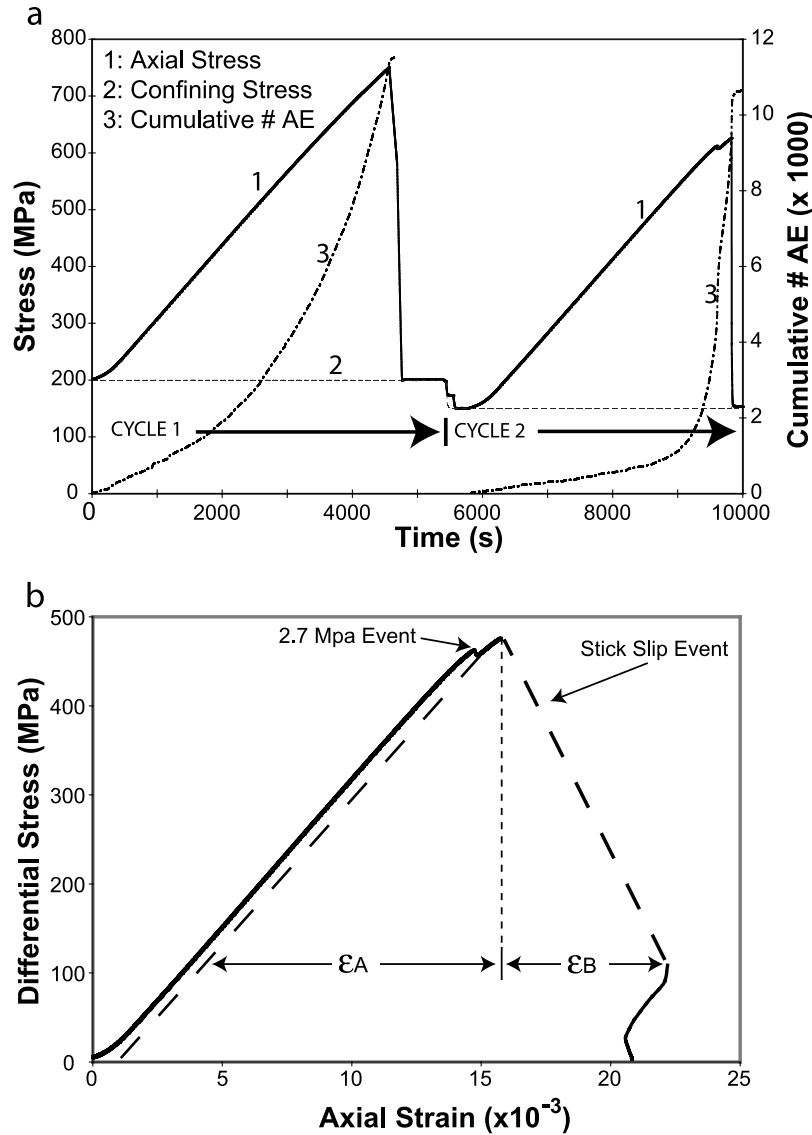


Figure 4. (a) Axial (1) and confining (2) stress with time for the two loading cycles ($P_c = 200$ MPa for cycle 1, $P_c = 150$ MPa for cycle 2), with the number of cumulative AE (3) for each loading cycle displayed on the secondary axis. (b) Differential stress ($\sigma_1 - \sigma_3$) versus axial strain for the second loading cycle. The stick-slip and elastic unloading portion of cycle 2 is dashed. Elastic and dynamic strains (ϵ_A and ϵ_B) are measured as 10.7×10^{-3} and 6.5×10^{-3} , respectively.

earthquake. We follow a procedure presented by *McGarr and Fletcher* [2003]. Seismic moment is normally computed from

$$M_0 = GuA \quad (1)$$

where G is shear modulus (~ 33 GPa for Westerly granite), u is displacement and A is fault surface area. However, equation (1) represents moment release for a fault embedded in an elastic medium. The equivalent radius, r , for a circular asperity with elastic unloading stiffness k is given by [*Eshelby, 1957; Walsh, 1971*]

$$r = (7\pi/16)G/k \quad (2)$$

Using values for the stick-slip event, the equivalent radius fault patch is 1.05 m ($A = 3.5$ m²). This is about 390 times

the area of the actual stick-slip surface. Substitution into equation (1) yields a moment for an equivalent earthquake of $M_0 = 4.15 \times 10^8$ Nm. Moment magnitude for an equivalent earthquake is then calculated using the scaling relation [*Hanks and Kanamori, 1979*]

$$M_w = 2/3(\log_{10} M_0) - 6.07 \quad (3)$$

to be $M_w = -0.32$ for the stick-slip event.

3.2. Elastic Wave Velocities and AE Locations

[17] Elastic wave velocities are plotted with time and differential stress in Figure 5a. To avoid potentially obscuring waveform data of the stick-slip event with the external ultrasonic source, velocities were measured only up to a differential stress of 400 MPa, above which point failure

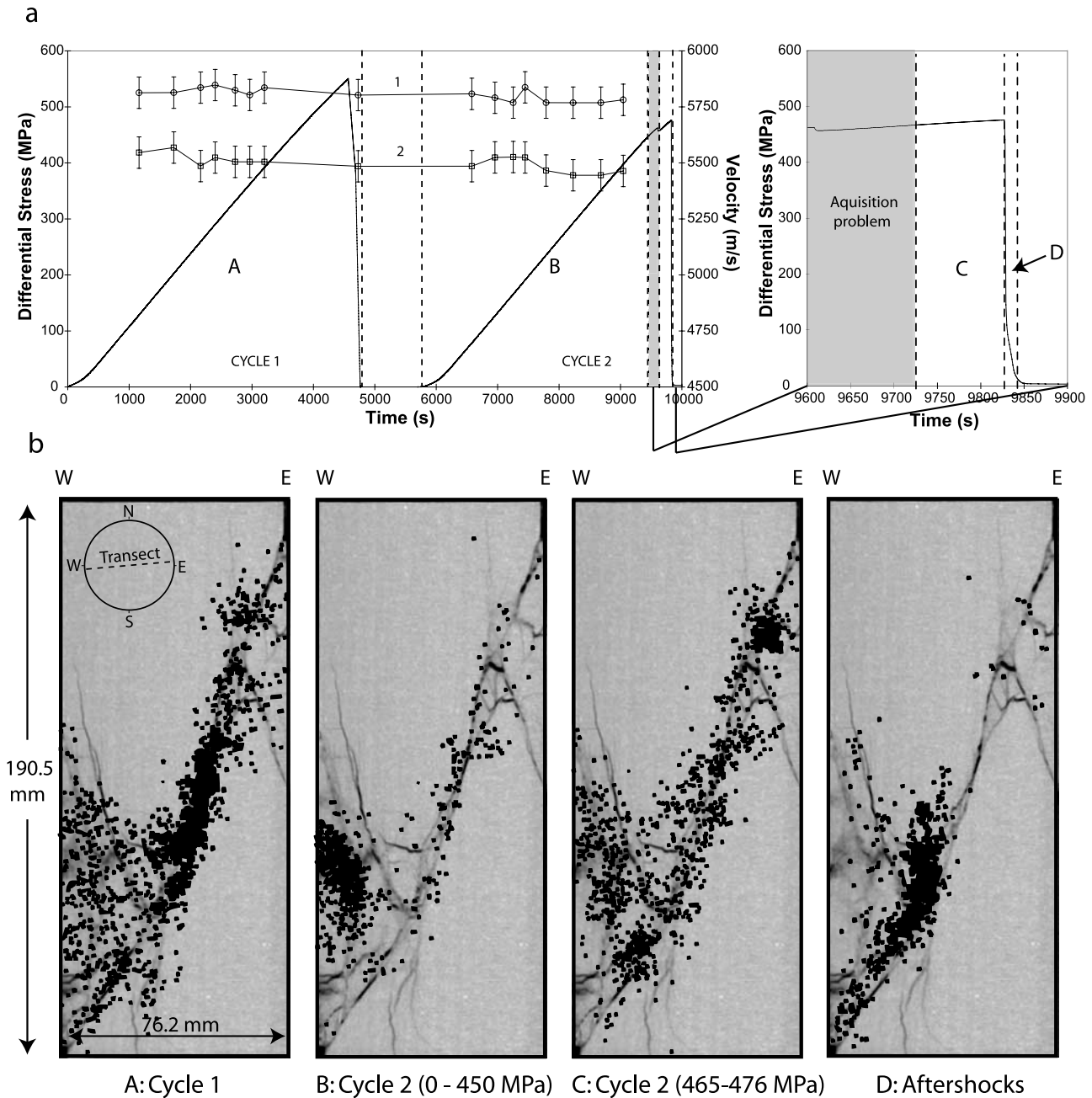


Figure 5. (a) Evolution of elastic wave velocities during loading cycles 1 and 2. The mean velocities of raypaths oriented at 50° and 90° to the sample axis are labeled (1) and (2), respectively. Error bars represent a picking accuracy of 1 sample point (± 70 m/s). (b) AE source locations from the entire experiment, with periods A–D marked in Figure 5a. AE are sampled from the same volume and superimposed onto the same CT image as in Figure 1.

was thought imminent. The mean velocity was 5825 m/s and 5500 m/s for raypaths inclined at angles of 50° and at 90° (radial) to the sample axis. Each plotted point corresponds to the mean value of four transmitter-receiver pairs. An estimated ± 70 m/s error in velocity based on a 1 sample point picking accuracy is indicated on Figure 5a and the variation in velocity measured during the test is sufficiently small to be within these error bounds. The velocity measurements are used to define the velocity model in the AE source location inversion. In the initial fracture experiment a

35 percent P wave velocity anisotropy developed prior to fault formation [Thompson *et al.*, 2006]. However the P-wave anisotropy plotted in Figure 5a is significantly smaller (approximately 13 percent) and shows little sensitivity to stress state. The 3- to 4-fold increase in confining pressure in the stick-slip portion of the experiment presented in this paper has closed existing microcracks and suppressed further crack growth away from the fracture zone. Instead, crack growth is confined to the fault zone, which comprises

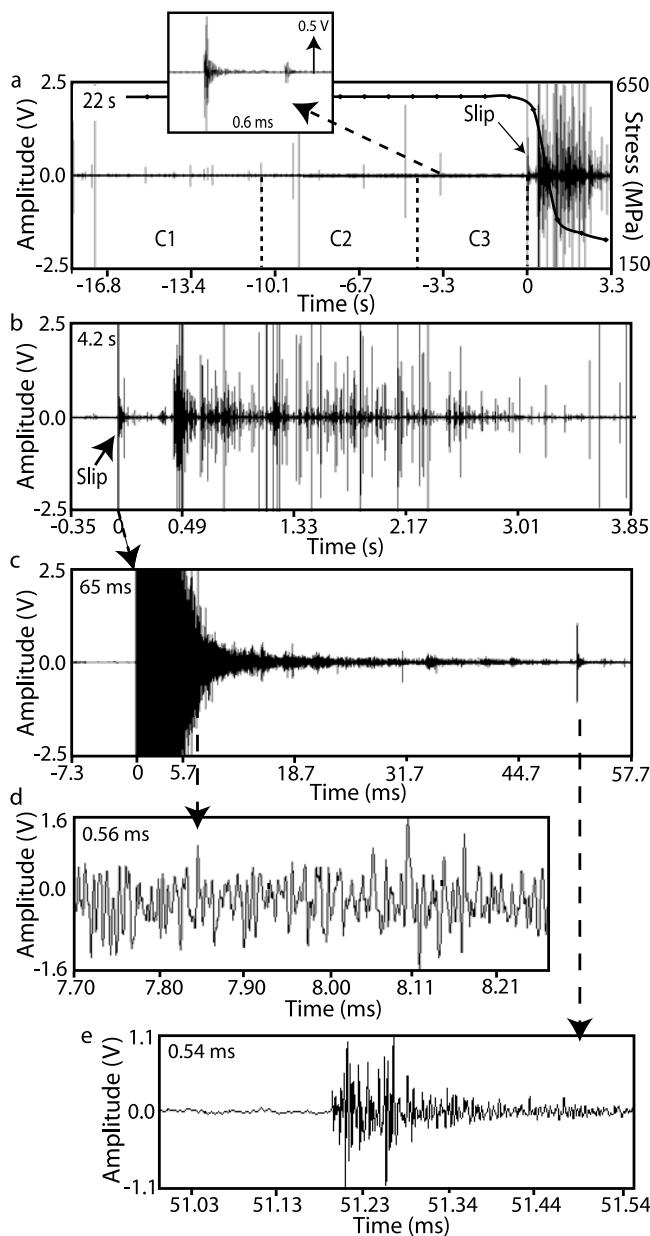


Figure 6. Summary continuous waveforms from a channel amplified at 20 dB. (a) A 22-s period of waveform data, plotted with stress. The initiation of stick-slip instability is indicated and a large AE ~ 3.3 s prior to slip expanded. Periods C1–C3 refer to location periods on Figure 8. (b) The waveform shows a 4.2-s period of activity. (c) First response of the stick-slip for a 65-ms period. (d, e) Detail expanded from Figure 6c.

a small fraction of the total sample volume, thus limiting the development of additional stress-induced anisotropy.

[18] AE source locations for the entire experiment are displayed in Figure 5b. Locations are divided into periods A to D, the timings of which are marked on Figure 5a (the final 300 s of the graph is expanded to show periods C and D). Data presented for periods A and B were collected using triggered AE, while AE events for periods C and D were extracted from the continuous waveform. In order to relate

the AE to physical features within the sample, AE locations are superimposed onto the CT image of the fault used in Figure 1. As in Figure 1, only AE occurring ± 10 mm from the plane of the CT image are presented. AE from the first loading cycle at 200 MPa confining pressure are shown in period A. These AE align with the main fault plane as well as filling a diffuse zone in the lower west quadrant of the sample that corresponds to a region of complex faulting. Period B includes the second loading cycle at $P_c = 150$ MPa up to a differential stress of 445 MPa. These AE highlight a more localized structure in the lower west quadrant of the sample near the sample surface and away from the main fault. Period B shows significantly less activity on the main fault plane than period A. Unfortunately there was a hardware problem which prevented the acquisition of AE data for 275 s following the end of period B, and so AE related to the 2.7 MPa stress drop were not recorded. Period C shows AE activity occurring in the 102 s leading up to the main stick-slip instability. A significant reactivation of the main fault plane has occurred. This is most likely an example of the Kaiser effect where, following the initial high stress state achieved during cycle 1 (period A), little additional AE could occur until the fault approached failure (period C). Much of the activity near the main fault appears in clusters. There is also AE activity in the lower west quadrant of the sample, although this is less dense and less structurally defined than during period B. The main stick-slip instability, representing slip on the entire main fault surface, occurs at the end of period C. Similar to aftershocks following a large earthquake, period D shows AE occurring after the stick-slip instability.

3.3. Continuous Waveform Data

[19] Summary plots of the continuous ultrasonic waveform recorded around the time of the stick-slip instability can provide qualitative understanding of the sample's behavior. Figure 6 shows summary waveforms for a channel near the center of the sample with 20 dB amplification. Timescales for these waveforms are relative to the initiation of the stick-slip instability. Figure 6a shows a 22-s period, for which stress is also plotted. In the 18.7 s before the dynamic slip instability there are a small number of AE. There is a sudden increase in amplitude which coincides with the stress drop (within the ± 1 -s time resolution of the stress/displacement data). This amplitude increase is interpreted as the initiation of the stick-slip instability (the waveforms associated with the stick-slip instability are termed the stick-slip event henceforth). Prior to this, no AE are indicated on this record for ~ 3.3 s, with the last, regular sized AE event expanded in the insert. Figure 6b shows a 4.2-s record that includes the stick-slip event. Following the initial slip pulse that lasted for about 8 ms, there was a 0.4-s period of significantly reduced acoustic noise. Then, activity again increased, providing numerous discrete AE events that could be located as aftershocks in Figure 5, period D. Further details of the stick-slip event are shown in Figure 6c for a 65 ms period. The first radiated energy of the stick-slip instability exceeded the dynamic range of the system for about 5 ms, after which the amplitude gradually decreased, with the signal appearing as high-amplitude noise (Figure 6d). After approximately 50 ms, a discrete AE was observed (Figure 6e).

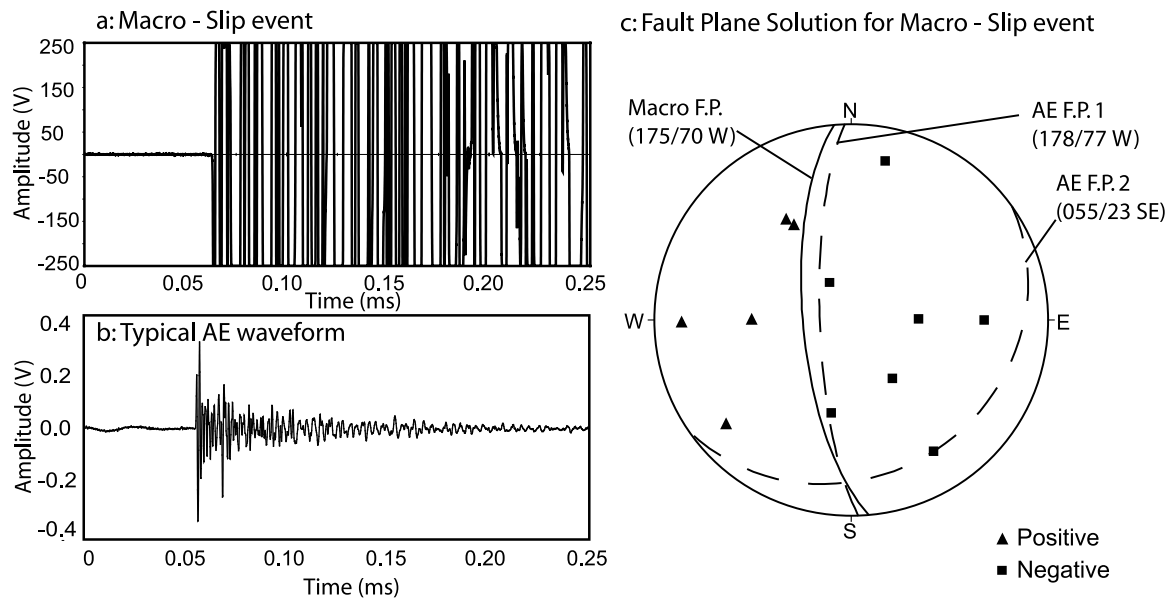


Figure 7. (a) The stick-slip event captured as an AE and (b) a typical AE event for comparison purposes. The amplitude scale of the waveform in Figure 7a has been increased by a factor of 10 in order to present the two waveforms on the same scale. In Figure 7c the fault plane solution for the stick-slip event is calculated using first motion polarity (dashed lines), with the orientation of the upper portion of the main fault plotted for comparison (solid lines).

3.4. Stick-Slip Event

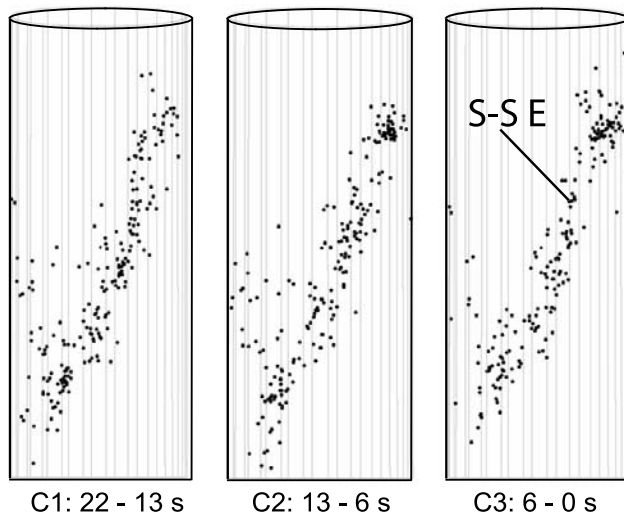
[20] The stick-slip event manifests as an abrupt increase in amplitude, exceeding the dynamic range of the recording system on all channels. In the future, the recording system will be optimized to record the maximum amplitudes of very large events. However, in this experiment the duration of the clipped portion of the waveform for the low gain (20 dB) channel is used as a rough guide to relative magnitudes. For the stick-slip event, the recorded ultrasonic amplitude exceeds the dynamic range of the system for a period of about 5 ms. The 2.7 MPa stress drop event that occurred 220 s before the stick-slip event was also followed by very large amplitude AE which exceeded the system's dynamic range for less than 1 ms. Approximately 2 microns of average axial shortening occurred during the 2.7 MPa event, as measured by a displacement sensor outside of the pressure vessel. As discussed in section 3.1, slip on the main fault would unload the sample at a rate of 43 MPa/mm shear stress (or 104 MPa/mm differential stress). The observed 2.7 MPa differential stress drop would require 26 microns of axial displacement, an amount that was not observed. We believe that the 2.7 MPa event represents slip on a secondary fault that developed in the lower left quadrant as indicated by the high rate of AE activity shown in Figure 5, period B. During the 219-s period before the stick-slip event, six more large amplitude AE events exceeded the system's dynamic range for periods of less than 0.2 ms. Large AE were also recorded during the aftershock sequence illustrated in Figure 6b and were less than 0.2 ms in duration. Therefore the stick-slip event was significantly larger than any other AE with the next largest AE events coinciding with the 2.7 MPa stress drop that was, in some sense, a foreshock of the stick-slip event. No other AE event resulted in measurable recorded stress drop.

[21] The first motions of the stick-slip event were extracted from the continuous ultrasonic record and were processed as a conventional AE. A comparison of the stick-slip event and a typical AE is presented in Figure 7. First arrival times were used to calculate the source location, which is interpreted as the nucleation site of the stick-slip instability. The fault plane solution for the stick-slip event is calculated from first arrival polarities of the ultrasonic waveforms, and is plotted in Figure 7c. Great circles representing the orientation of the main fault are measured from the CT images and plotted on the stereonet, with dips ranging between 55° and 78° . The stick-slip event's westerly dipping fault plane has similar orientation to the main fault, as consistent with this event representing the initiation of the stick-slip instability.

3.5. Source Locations of the Main Stick-Slip Event and Premontory AE

[22] Figure 8 displays AE locations from the 22 s prior to the stick-slip initiation. Events are divided into time periods C1, C2, and C3, as marked on Figure 6a. Each period contains 202 events. AE are displayed from the entire sample volume, and viewed (1) along strike in Figure 8a and (2) perpendicular to the strike of the fault plane in Figure 8b. In C1, AE are distributed over the entire fault. In C2, again AE locate on the fault, with a cluster developing near the top extent of the main fault. A similar pattern is observed in C3. The duration of plot windows C1 through C3 indicates a steadily increasing event rate leading up to macroscopic fault slip, i.e., 202 events in 9, 7 and 6 s respectively. This event rate is very low in comparison to intact fracture tests [i.e., Thompson *et al.*, 2006]. The stick-slip event location that marks the nucleation site of the stick-slip instability is indicated on Figure 8.

a) View along strike of fault plane:



b) View into fault plane:

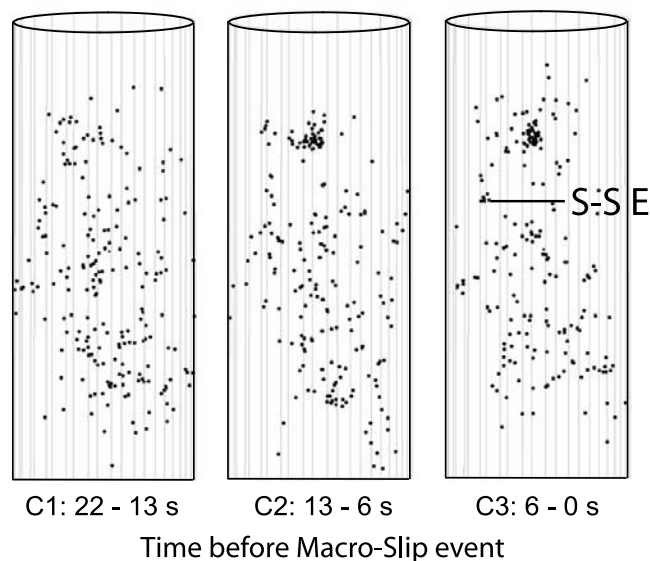


Figure 8. AE locations shown for 22 s prior to the stick-slip event, viewed (a) along strike and (b) perpendicular to the strike of the fault. Each of periods C1–C3 contain 202 events, and the stick-slip event is indicated in C3 (marked S-S E). The timing of periods C1–C3 is marked in Figure 6a.

[23] AE locations are superimposed onto CT images of the sample in Figure 9. Three mutually perpendicular planes are displayed (P 1–3), with each passing through the source location of the stick-slip event. P1 is the along strike view, (AE locations are displayed for a volume ± 2 mm out of the plane of the CT image), in this case AE events occur primarily on the upper half of the main fault surface. Cluster 1 (marked on Figure 9) is associated with the intersection of the main and preexisting quasi-statically propagated secondary fault plane. Cluster 2 may also be associated with a secondary fault that connects these two faults. The nucleation site for the stick-slip event locates within this cluster as indicated. Cluster 3 is located at the midpoint of the main

fault. P2 is viewed perpendicular to the strike of the fault. AE are superimposed from a volume extending ± 2.5 mm from the plane of the image, limited by a vertical distance of ± 5 mm from the stick-slip nucleation site. The nucleation site locates within the cluster on the north side of the image. P3 shows a horizontal slice through the sample, with AE locations superimposed for events occurring within a volume extending ± 2 mm from the plane of the image. The orientations of transects P1 and P2 are marked on P3. In order to show details of the AE associated with the nucleation site, this region is highlighted in P3 and expanded in P3'. The nucleation event locates to the south of this cluster, close to a branch in the fault, within a region of high structural heterogeneity. We interpret this cluster of AE as indicating the existence of a high stress asperity.

3.6. AE Source Mechanisms

[24] The AE source mechanisms are classified into event types by converting the MT into three mutually orthogonal eigenvectors and corresponding eigenvalues. The former can be interpreted as the principal stress axes acting at a

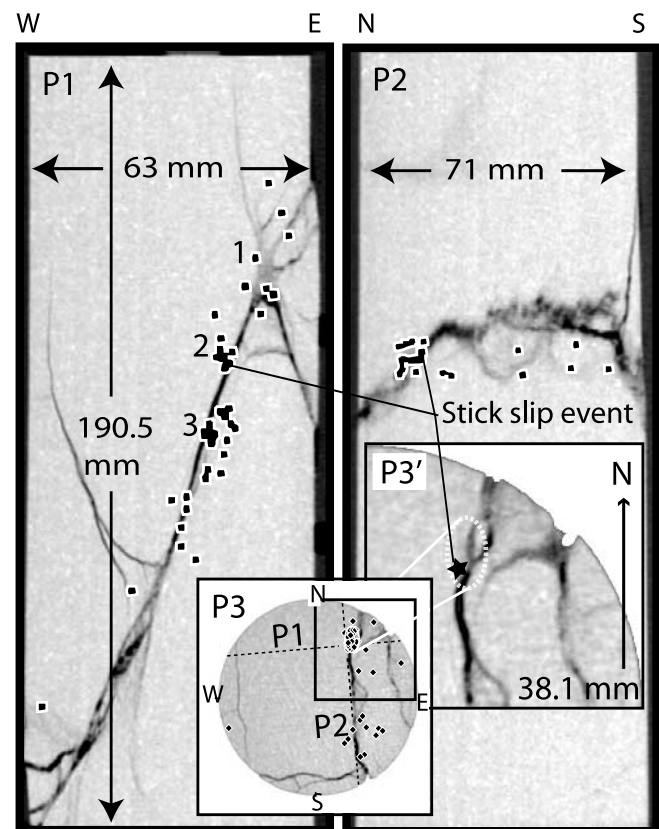


Figure 9. AE locations are superimposed onto CT images along three planes (P1–3) through the nucleation event source location to show the site of stick-slip nucleation and premonitory microcracking. (P1) The sample is viewed along strike of the main fault, with three regions of interest (1–3) marked. (P2) The sample is viewed perpendicular to the strike. P3 shows the horizontal slice. The cluster of AE about the stick-slip nucleation site is expanded in P3' to demonstrate the fault structure in this area. The orientations of transects P1 and P2 are marked on P3.

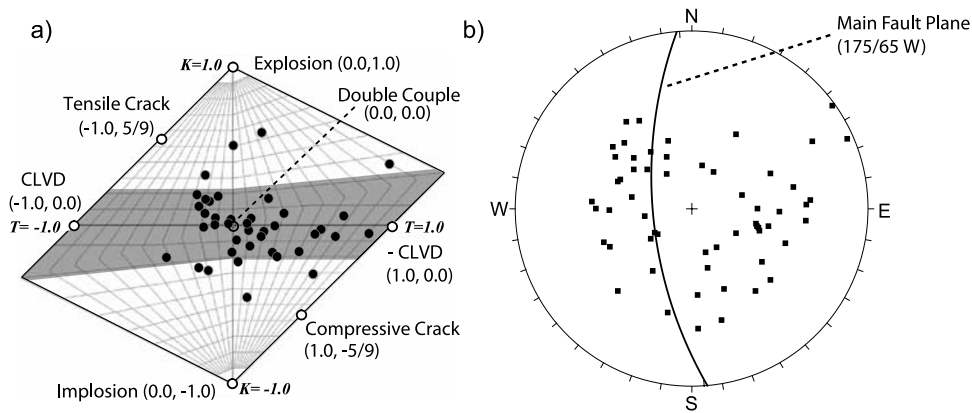


Figure 10. AE source mechanisms are calculated from moment tensor inversion of first arrival amplitudes for 40 of the largest events recorded before the stick-slip event. The mechanisms are displayed on a source-type diagram. Each shear type AE has two possible slip vectors, which are plotted on an equal angle stereonet along with the main fault plane.

source and the latter as the magnitude and polarity of the stresses. Source mechanism data are displayed on a Source Type plot [after Hudson *et al.*, 1989]. The volumetric component, k , is plotted on the vertical axis, and the deviatoric component, T is plotted on the horizontal axis. Both values are normalized to range between -1 and 1 . Following Collins *et al.* [2002] the volumetric component k is only considered significant if it is less than -0.22 or greater than 0.22 . The remaining region on the source type plot (Figure 10) is shaded grey and is interpreted to contain deviatoric sources only. The advantages of the source type plot are that many mechanisms can be presented on one diagram, and that their distribution can be compared with calculated source types (i.e., tensile (T), double couple (DC), and compensated linear vector dipole (CLVD)).

[25] Source mechanisms are calculated for the 40 largest events for which arrivals do not exceed the ± 2.5 V dynamic range during the second loading cycle. In general, events have small to insignificant volumetric components, clustering about the modeled DC source. Two possible slip vectors for each shear sourced AE are interpreted directly from the MT eigenvectors and plotted on an equal angle stereonet in Figure 10b, along with the great circle indicating the orientation of the main fault plane. The fault dips to the west, suggesting the true AE slip vectors plot in the western half of the stereonet. The slip vectors are scattered, as would be expected for the heterogeneous fault.

4. Discussion

4.1. Relationship of AE and Fault Topography

[26] Evidence of the role of secondary fault interaction with the main fault is provided by the distribution of AE activity before and after the 2.7 MPa stress drop that occurred 220 s prior to the slip-slip instability (Figure 5). As mentioned before, a problem with the acquisition system resulted in a 275-s gap in locating AE events that included the 2.7 MPa stress drop event. AE activity prior to this stress drop was concentrated within a region of secondary faulting with only minor activity on the main fault. After the 2.7 MPa stress drop AE are distributed more diffusely over a greater region of the secondary fault. Also, subsequent AE

activity greatly increased on the main fault plane. That the 2.7 MPa stress drop had almost no measurable change in axial strain indicates the main fault did not move. The intense AE activity prior to the 2.7 MPa stress drop is identical to AE recorded during fault nucleation that we have observed in both quasi-static and dynamic fault growth experiments. Fault nucleation in the initially intact sample, plotted in Figure 1, is an example of this AE pattern. We interpret the intense AE activity in Figure 5b, period B as the nucleation of a secondary fault in this region that became unstable and culminated in the 2.7 MPa dynamic stress drop event. This new secondary faulting was arrested when it intersected the main fault surface. This secondary fault was forced to develop because of the sharp bend in the existing main fault in the lower quadrant of the sample. At the elevated confining pressure in this experiment, the lower portion of the main fault was pinned at this bend and further slip could not occur until the conjugate secondary fault was formed. Then, as indicated by the AE pattern in Figure 5b, period C, both the main fault and the newly formed secondary fault accumulated microcrack damage with continued loading until nucleation of the main stick-slip event. We conclude that the high angle of the main fault and the elevated confining pressure meant that macroscale slip required cooperative slip on the main and conjugate fault.

[27] In Figure 11, the CT scan images are used to demonstrate how the complexity of the fault geometry controls the distribution of the microfracture events that manifest as AE. Three clusters of AE activity are selected from the 100-s interval preceding the main stick-slip event (period C, Figure 5). These clusters are superimposed on the expanded CT images in Figure 11. Clusters 1 and 2 occur where two separate secondary faults intersect the main fault. In the case of Cluster 3, a secondary fault is oriented subparallel to the main fault and is surrounded by a region of relatively heavy damage. The association of increased AE activity with fault junctions suggests that these fault intersections represent regions of stress concentration.

[28] Whilst the main fault plane remained locked until the stick-slip instability, AE along the fault, signifying microcrack damage accumulation did not occur uniformly. Rather, it was spatially clustered within areas of lower damage

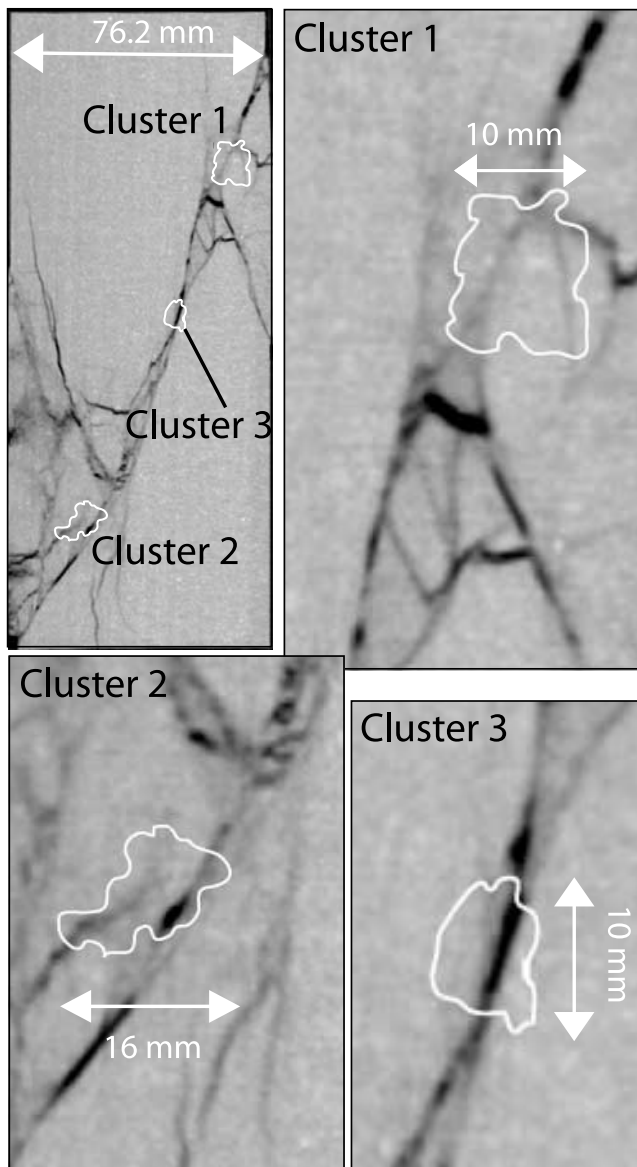


Figure 11. Magnified view of AE clusters from preslip AE source location data during period C of Figure 5. Clusters 1–3 are indicated as regions of high activity on the main fault and are marked on the expanded CT images.

accumulation. Our interpretation is that AE represent micro-scale stick-slip events or failure of interlocking asperities, and demonstrate the fractal nature of faulting, consistent with the observations of *Lei et al.* [2003]. The regions of sparse AE activity probably experience smaller stresses due to the presence of nearby asperities. On the field scale, microseismic events are frequently observed on creeping faults, and improvements in location techniques have demonstrated these form streaks of microearthquakes that are thought to be separated by locked regions [*Waldhauser and Ellsworth, 2002*]. We suggest that by combining AE and CT mapping of a natural fault, we have demonstrated a laboratory analogue of a partially locked fault zone.

4.2. Stick-Slip on Natural and Saw-Cut Fault Planes

[29] *Thompson et al.* [2005] demonstrated the AE characteristics of a sample containing a saw-cut, “smooth” fault plane on which three stick-slip events were induced. The sample size, lithology, and experimental configuration were identical to those of the naturally faulted sample, to facilitate comparison of the manifestation of dynamic instabilities on geometrically simple and complex laboratory fault planes.

[30] Mechanical data, frictional coefficients and seismic moments and magnitudes from the two stick-slip experiments are compared in Table 1. The mean values of peak differential stresses and frictional coefficients are 263 MPa and 0.53 for the saw cut faulted sample and 476 MPa and 0.78 for the natural fault. An error was found in the original estimates of fault displacement for the saw-cut sample in the work of *Thompson et al.* [2005] and these values have been revised as 0.94, 0.89 and 1.23 mm, including a correction for the elastic rebound of the sample. The mean displacement is 1.02 mm, and this value is used with equations (1) and (3) using a shear modulus of 33 GPa and a fault area of 3.5 m², calculated from the equivalent radius fault patch (equation (2)) to provide an equivalent seismic moment (for a circular crack in the earth adjusted for the stiffness of the triaxial loading frame) of 1.18×10^8 Nm and a moment magnitude of -0.69 (see section 3.1). The equivalent seismic moment and moment magnitude of the natural fault were calculated as $M_0 = 4.15 \times 10^8$ Nm and $M_w = -0.32$.

[31] AE locations prior to the first stick-slip event on the saw-cut plane were distributed about the fault tips (Figure 12a) because of compaction of sand infilling placed in these regions. The sand was required to fill the volumes created by the destruction of the fault tips during the saw-cutting process. The first of the three stick-slip events nucleated about the lower fault tip. For the second and third slip events on the saw cut fault plane, premonitory AE locate mainly in a cluster on the lower fault plane (Figure 12b). The second slip event nucleated at the edge of the sample and the third slip event nucleated at the edge of the AE cluster on the lower half of the fault.

[32] Whereas thousands of AE are located on the natural fault plane, fewer than one hundred AE locate on the saw-cut plane. The limited clustering of AE in the later case reflects the homogeneity of the smooth fault surface, with

Table 1. Parameters Calculated During Stick-Slip Experiments on Samples Containing Rough, Naturally Formed, and Smooth, Saw-Cut Faults

Fault Type	Natural/Rough	Saw-Cut			
		1	2	3	Mean
Stick-Slip Event					
Peak differential stress (MPa)	476	230	251	310	263
Static coefficient of friction ^a	0.78	0.48	0.51	0.59	0.53
Displacement on fault (mm) ^b	3.61	0.94	0.89	1.23	1.02
Equivalent seismic moment (Nm) $\times 10^8$	4.15	1.08	1.03	1.42	1.18
Moment magnitude	-0.32	-0.71	-0.73	-0.64	-0.69

^aRatio of shear and normal stress resolved onto the fault plane.

^bResolved from axial displacement with component of elastic unloading removed.

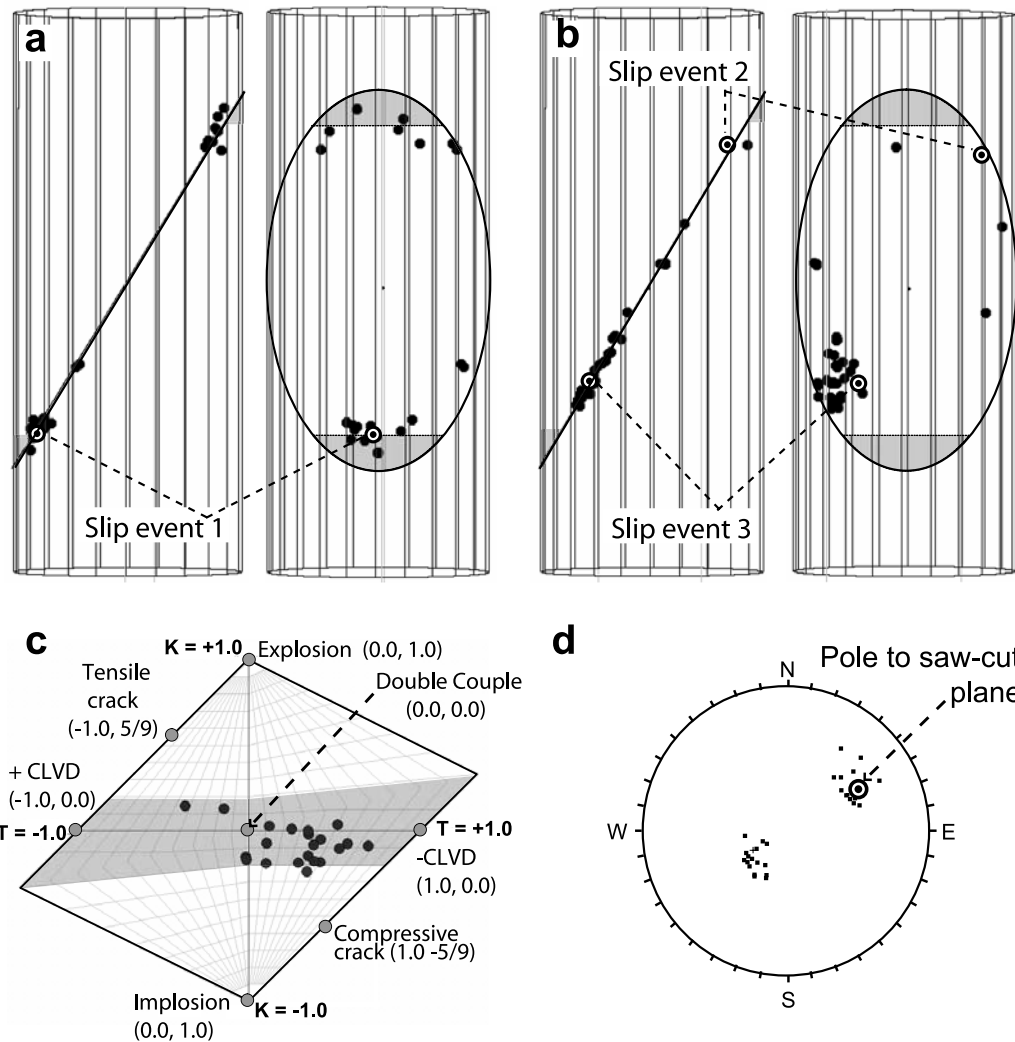


Figure 12. AE locations from a stick-slip test on a smooth, saw-cut fault plane. (a) AE locations premonitory to the first stick-slip event. (b) AE locations premonitory to second and third slip events. The nucleation site of the three slip events is indicated with double circles. (c) Source mechanisms for AE premonitory to slip events two and three. (d) Slip vectors of dominantly shear AE events are presented on an equal angle stereonet, with the slip vector of the saw-cut fault indicated. Adapted from the work of *Thompson et al.* [2005].

the sole AE cluster indicating a region of stress concentration. The close proximity of the third slip event to this cluster suggests a relationship between nucleation of slip and the asperity. Source mechanisms for AE occurring before the second and third stick-slip events can mostly be modeled as having dominantly shear sources (Figure 12c). Two possible slip vectors can be calculated from each shear source modeled MT, these are plotted on the stereonet in Figure 12d and show close agreement with the slip vector of the saw-cut fault plane. In comparison with MT of AE from the natural fault, MT of AE from the saw-cut fault have a smaller range of volumetric components and their slip vectors align more closely to the slip plane of the main fault. These differences are consistent with the differences in fault complexity and heterogeneity.

[33] Ultrasonic waveforms of duration 16.7 and 1.05 s are compared in Figure 13 for stick-slip events on the smooth and natural faults, and also for failure of an intact sample of

Westerly granite [*Thompson et al.*, 2006]. Unlike Figure 6, these waveforms are from channels amplified at 40 dB, in order to emphasize details of foreshocks. Scrutiny of the 16.7-s period highlights the significant difference in quantity of premonitory AE between the two stick-slip experiments. However, as can be seen from the 1.05-s duration waveforms, there are close similarities in the ultrasonic signature of initiation of the slip events in terms of onset and duration. The high-energy aftershock sequence observed for the natural fault is not present on the ultrasonic record of the saw-cut fault presumably because of the relative lack of asperities on the saw-cut fault surface as stress relaxation and subsequent reloading occurs.

[34] The rapid increase in AE activity prior to fracture of the intact sample (Figure 13c) is related to the nucleation and initial propagation of the fault [*Thompson et al.*, 2006]. This stage is absent for the stick-slip experiments, as the slip nucleus is provided by a preexisting crack, consistent with

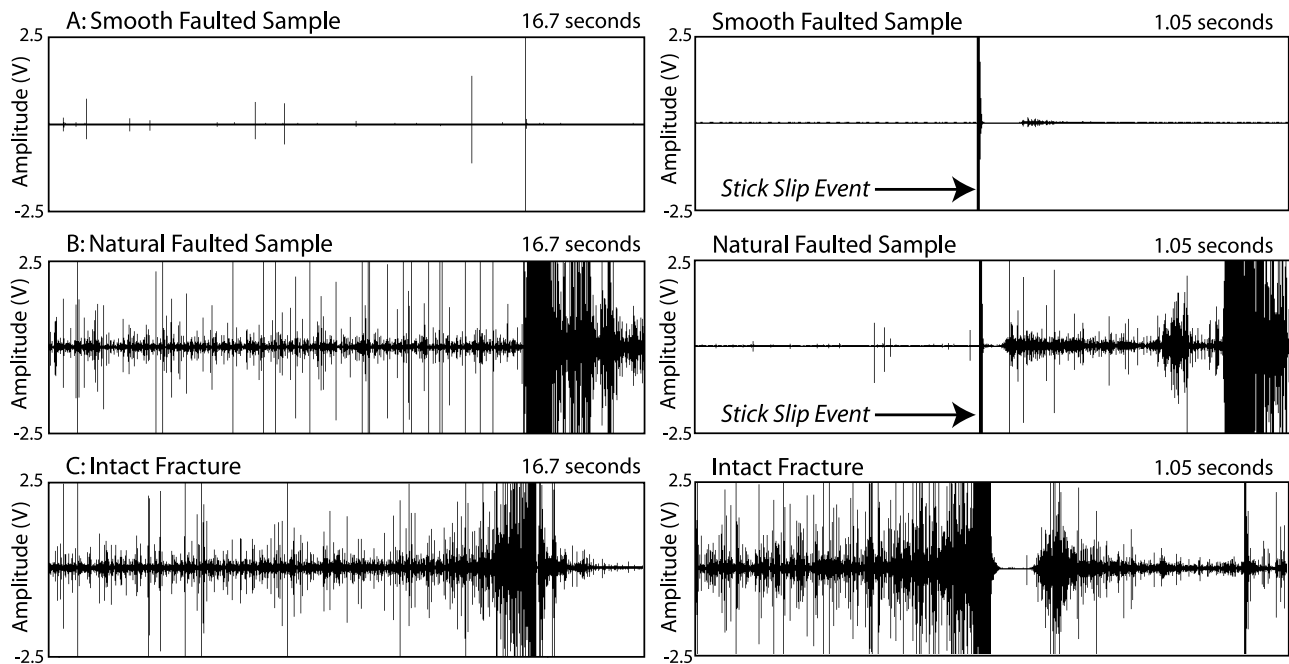


Figure 13. Summary continuous waveforms for (a) the smooth-faulted stick-slip, (b) natural-faulted stick-slip, and (c) failure of an intact sample, shown for 16.7- and 1.05-s periods. Contrary to Figure 6, the waveforms are amplified at 40 dB.

the observations of *Ohnaka and Kuwahara* [1990]. Unlike previous biaxial tests, premonitory creep was not observed in our stick-slip experiments, most likely suppressed by the high normal stresses in our tests. High-resolution strain measurements will be applied in future experiments.

4.3. Stick-Slip and Intact Fracture in the Laboratory

[35] Earthquake nucleation characteristics have been likened to fracture nucleation in intact rocks [*Reches*, 1999] and similarities in the nucleation processes of fracture and frictional slip have been demonstrated in the laboratory [*Ohnaka*, 2003; *Thompson et al.*, 2006]. *Reches* [1999] proposes that earthquake nucleation occurs by the interaction of multiple fractures within a small volume. From this, unstable yielding of the healed fault zone occurs. Experiments to investigate interaction between processes of frictional slip and fracture of intact rock have potential in providing information about earthquake nucleation. Figure 13 provides a direct comparison between the ultrasonic records of both of these processes highlighting the significant difference in premonitory activity. Triaxial failure experiments upon samples containing healed joints have been performed by *Jouniaux et al.* [2001] and *Lei et al.* [2003, 2004] using confining stresses of 40 and 60 MPa respectively. *Lei et al.* [2003] demonstrated that AE patterns followed a similar trend to failure of intact samples, in terms of prenucleation AE distributed throughout samples, and events associated with nucleation locating on the fault plane. In the nucleation stage, AE clusters of diameter <30 mm are demonstrated, which represent asperities on the fault plane. As asperities failed they transferred stress to neighboring asperities. *Lei et al.* [2003] interpreted their progressive failures as a quasi-static nucleation phase, preceding the dynamic rupture of the fault, and thus demon-

strating the hierarchical nature of faulting. Our study differs in the nature of the preexisting plane of weakness and in the higher applied confinement. A future research aim is to further explore these variables using continuously recorded AE in order to distinguish a transition between the nucleation of stick-slip like frictional instability and intact fracture, in terms of the premonitory AE activity and ultrasonic records of failure.

5. Conclusion

[36] A combination of AE and CT imaging has been used in a stick-slip experiment performed on a geometrically complex fault plane to correlate the temporal and spatial evolution of AE with physical features of the fault plane. In this sample, interaction between the main fault and secondary faults was a controlling factor in the evolution of stress concentration within the sample. Clusters of AE are associated with inflection points on the main fault, and secondary fault intersections, which act as stress concentrators or asperities, and play a key role in resisting the onset of the large-scale slip event. In this regard, we consider this experiment a laboratory analogue of a partially locked fault zone. There are similarities in the pattern of precursory seismic activity between the field scale and the stick-slip experiments described here. Prior to the stick-slip event, a pattern of increasing AE activity is observed in the long term (100s of seconds). However, in the short term (10s of seconds) there are no immediate precursors to the slip event. As on the field scale, this presents a significant obstacle to short-term prediction of the stick-slip event. The moment magnitudes of the laboratory stick-slip events are in the mining-induced microseismic range [*Boettcher et al.*, 2007; *Feignier and Young*, 1992], thus the nucleation and source

properties of the events described here can be directly compared to natural events.

[37] The combination of AE and CT imaging provides a powerful analytical tool that enables a more complete qualitative understanding of rupture surface processes prior to dynamic instabilities in the laboratory. Analysis of earthquake nucleation and dynamic rupture requires understanding of complex fault system behavior. We have shown that a naturally fractured laboratory sample can provide an analogue for complex fault systems on the field scale, and can lead to a better understanding of how microstructural behavior, fault strength and the nucleation of instabilities are affected by fault zone complexity.

[38] **Acknowledgments.** The authors would like to thank G. Dresen, F. Waldhauser, N. Beeler, and M. Boettcher for very constructive reviews, and D. Collins, P. Benson, A. McGarr, and A. Schubnel for their useful comments and discussions. The assistance of R. Ketcham (University of Texas at Austin) in providing high-resolution CT images, and R. Bowes (Engineering Seismology Group, Inc.) and W. Pettitt (Applied Seismology Consultants, Ltd.) for experimental and software assistance is gratefully acknowledged. This work was made possible by a National Environment Research Council equipment grant, in partnership with ESG, and was partially funded by the University of Liverpool and the Natural Sciences and Engineering Research Council of Canada (Discovery Grant to Young).

References

- Benson, P. M., B. D. Thompson, P. G. Meredith, S. Vinciguerra, and R. P. Young (2007), Imaging slow failure in triaxially deformed Etna basalt using 3D acoustic-emission location and X-ray computed tomography, *Geophys. Res. Lett.*, *34*, L03303, doi:10.1029/2006GL028721.
- Ben-Zion, Y. (2001), Dynamic ruptures in recent models of earthquake faults, *J. Mech. Phys. Solids*, *49*, 2209–2244.
- Ben-Zion, Y., and C. G. Sammis (2003), Characterization of fault zones, *Pure Appl. Geophys.*, *160*, 677–715.
- Boettcher, M. S., A. McGarr, and M. Johnston (2007), A search for minimum-magnitude earthquakes in South African gold mines, *Seismol. Res. Lett.*, *78*(2), 293.
- Brace, W. F., and J. D. Byerlee (1966), Stick-slip as a mechanism for earthquakes, *Science*, *153*(3739), 990–992.
- Brown, S. R., and C. H. Scholz (1985), Broad bandwidth study of the topography of natural rock surfaces, *J. Geophys. Res.*, *90*(B14), 12,575–12,582.
- Collins, D. S., W. S. Pettitt, and R. P. Young (2002), High-resolution mechanics of a microearthquake sequence, *Pure Appl. Geophys.*, *159*(1–3), 197–219.
- Dieterich, J. H. (1978), Time-dependent friction and mechanics of stick-slip, *Pure Appl. Geophys.*, *116*(4–5), 790–806.
- Dieterich, J. H. (1979), Modeling of rock friction: 1. Experimental results and constitutive equations, *J. Geophys. Res.*, *84*(B5), 2161–2168.
- Eshelby, J. (1957), The determination of the elastic field of an ellipsoidal inclusion and related problems, *Proc. R. Soc. London Ser. A*, *241*, 376–396.
- Feignier, B., and R. P. Young (1992), Moment tensor inversion of induced microseismic events: Evidence of non-shear failures in the $-4 < M < -2$ moment magnitude range, *Geophys. Res. Lett.*, *19*(14), 1503–1506.
- Hanks, T. C., and H. Kanamori (1979), Moment magnitude scale, *J. Geophys. Res.*, *84*(B5), 2348–2350.
- Hudson, J. A., R. G. Pearce, and R. M. Rogers (1989), Source type plot for inversion of the moment tensor, *J. Geophys. Res.*, *94*(B1), 765–774.
- Jouniaux, L., K. Masuda, X. L. Lei, O. Nishizawa, K. Kusunose, L. Q. Liu, and W. T. Ma (2001), Comparison of the microfracture localization in granite between fracturation and slip of a preexisting macroscopic healed joint by acoustic emission measurements, *J. Geophys. Res.*, *106*(B5), 8687–8698.
- Kato, N., T. Satoh, X.-L. Lei, and T. Hirasawa (1999), Effects of fault bend on the rupture propagation process of stick-slip, *Tectonophysics*, *310*, 81–99.
- Ketcham, R. A., and W. D. Carlson (2001), Acquisition, optimization and interpretation of X-ray computed tomographic imagery: Applications to the geosciences, *Comput. Geosci.*, *27*, 381–400.
- Lei, X.-L., K. Kusunose, T. Satoh, and O. Nishizawa (2003), The hierarchical rupture process of a fault: An experimental study, *Phys. Earth Planet. Inter.*, *137*(1–4), 213–228.
- Lei, X.-L., K. Masuda, O. Nishizawa, L. Jouniaux, J. Q. Liu, W. T. Ma, T. Satoh, and K. Kusunose (2004), Detailed analysis of acoustic emission activity during catastrophic fracture of faults in rock, *J. Struct. Geol.*, *26*(2), 247–258.
- Lockner, D. A., and N. M. Beeler (2002), Rock failure and earthquakes, in *International Handbook of Earthquake and Engineering Seismology*, edited by W. H. K. Lee et al., pp. 505–537, Elsevier, New York.
- Louis, L., T. F. Wong, P. Baud, and S. Tembe (2006), Imaging strain localization by X-ray computed tomography: Discrete compaction bands in Diemelstadt sandstone, *J. Struct. Geol.*, *28*, 762–775.
- McGarr, A. (1999), On relating apparent stress to the stress causing earthquake fault slip, *J. Geophys. Res.*, *104*(B2), 3003–3011.
- McGarr, A., and J. B. Fletcher (2003), Maximum slip in earthquake fault zones, apparent stress, and stick-slip friction, *Bull. Seismol. Soc. Am.*, *93*(6), 2355–2362.
- Nelder, J. A., and R. Mead (1965), A Simplex-method for function minimization, *Comput. J.*, *7*(4), 308–313.
- Ohnaka, M. (2003), A constitutive scaling law and a unified comprehension for frictional slip failure, shear fracture of intact rock, and earthquake rupture, *J. Geophys. Res.*, *108*(B2), 2080, doi:10.1029/2000JB000123.
- Ohnaka, M., and Y. Kuwahara (1990), Characteristic features of local breakdown near a crack-tip in the transition zone from nucleation to unstable rupture during stick-slip shear failure, *Tectonophysics*, *175*(1–3), 197–220.
- Okubo, P. G., and J. H. Dieterich (1984), Effects of physical fault properties on frictional instabilities produced on simulated faults, *J. Geophys. Res.*, *89*(B7), 5817–5827.
- Power, W. L., T. E. Tullis, S. Brown, G. N. Boitnott, and C. H. Scholz (1987), Roughness of natural fault surfaces, *Geophys. Res. Lett.*, *14*(1), 29–32.
- Reches, Z. (1999), Mechanisms of slip nucleation during earthquakes, *Earth Planet. Sci. Lett.*, *170*(4), 475–486.
- Rice, J. R., and M. Cocco (2007), Seismic fault rheology and earthquake dynamics, in *Tectonic Faults: Agents of Change on a Dynamic Earth*, edited by M. R. Handy, G. Hirth, and N. Hovius (Dahlem Workshop 95, Berlin, January 2005 on the Dynamics of Fault Zones), chap. 5, pp. 99–137, MIT Press, Cambridge, Mass.
- Rubin, A. M., D. Gillard, and J. L. Got (1999), Streaks of microearthquakes along creeping faults, *Nature*, *400*(6745), 635–641.
- Ruina, A. (1983), Slip instability and state variable friction laws, *J. Geophys. Res.*, *88*(B12), 10,359–10,370.
- Stanchits, S. A., D. A. Lockner, and A. V. Ponomarev (2003), Anisotropic changes in P-wave velocity and attenuation during deformation and fluid infiltration of granite, *Bull. Seismol. Soc. Am.*, *93*(4), 1803–1822.
- Thompson, B. D., R. P. Young, and D. A. Lockner (2005), Observations of premonitory acoustic emission and slip nucleation during a stick slip experiment in smooth faulted Westerly granite, *Geophys. Res. Lett.*, *32*, L10304, doi:10.1029/2005GL022750.
- Thompson, B. D., R. P. Young, and D. A. Lockner (2006), Fracture in Westerly granite under AE feedback and constant strain rate loading: Nucleation, quasi-static propagation, and the transition to unstable fracture propagation, *Pure Appl. Geophys.*, doi:10.1007/s00024-006-0054.
- Udias, A., and E. Buforn (1988), Single and jointed fault plane solutions from first motion data, in *Seismological Algorithms*, edited by D. J. Doornbos, pp. 443–453, Elsevier, New York.
- Waldhauser, F., and W. L. Ellsworth (2002), Fault structure and mechanics of the Hayward Fault, California, from double-difference earthquake locations, *J. Geophys. Res.*, *107*(B3), 2054, doi:10.1029/2000JB000084.
- Walsh, J. B. (1971), Stiffness in faulting and friction experiments, *J. Geophys. Res.*, *76*(35), 8597–8598.
- Yoshida, S., and A. Kato (2001), Single and double asperity failures in a large-scale biaxial experiment, *Geophys. Res. Lett.*, *28*(3), 451–454.

D. A. Lockner, U.S. Geological Survey, 345 Middlefield Road, MS/977 Menlo Park, CA 94025, USA.

B. D. Thompson and R. P. Young, Department of Civil Engineering, Lassonde Institute, University of Toronto, 170 College Street, Toronto, ON M5S 3E3, Canada. (ben.thompson@utoronto.ca)